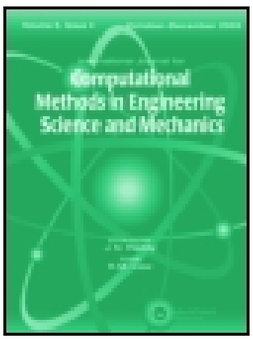

International Journal for Computational Methods in Engineering Science and Mechanics

ISSN: 1550-2287 (Print) 1550-2295 (Online) Journal homepage: http://www.tandfonline.com/loi/ucme20

A large strains finite element multiscale approach

A.J. Carneiro Molina & J.L. Curiel-Sosa

To cite this article: A.J. Carneiro Molina & J.L. Curiel-Sosa (2016): A large strains finite element multiscale approach, International Journal for Computational Methods in Engineering Science and Mechanics, DOI: 10.1080/15502287.2016.1145761

To link to this article: http://dx.doi.org/10.1080/15502287.2016.1145761

Accepted author version posted online: 06 Feb 2016.

A large strains finite element multiscale approach

A.J. Carneiro Molina[a], J.L. Curiel-Sosa[b]

[a]*Rockfield Sofware Ltd, Ethos, Kings Road, Swansea Waterfront, SA1 8AS, UK*

[b]*Department of Mechanical Engineering, University of Sheffield, Sir Frederick Mappin Bld, Sheffield S1 3JD, UK*

Abstract

A novel formulation for multiscale finite element analysis of multi-phase solids undergoing large strains is proposed in this paper. Within the described homogenization technique no constitutive assumptions are made at the macrolevel. A crucial aspects of the approach is the modelling of antiperiodic traction on the boundary of the representative volume element, condensation technique and the formulation performed on a deformation-driven context whereby the macroscopic deformation gradient is prescribed. Numerical tests on solids with voids demonstrated the robustness of the technique.

Keywords: large strain, voids, large deformation, plasticity, constitutive, thick cylinder

1. Introduction

There is a large number of references dealing with the modelling by multiscale techniques. However, only a few are dealing with large strains. Thus, there are multiscale approaches dealing with small strains [1, 2, 3, 4, 5, 6], ductile damage [7], plasticity [8, 9, 10], quasi-brittle materials [11, 12, 13, 14], laminates [15], filament–wound composites [16], shape memory alloy composites [17],randomly distributed heterogeneities [18], fracture [19, 20, 21, 22, 23, 24], fracturing reinforced composites based in an embedded cell methodology [25], for the solution of granular materials problems with periodically repeated aggregate configurations [26]. A computational multiscale technique using shells for system of heterogeneous thin sheets with in-plane quadrature points at the macroscale was proposed by [27]. They used the curvature of the shell to define the boundary conditions at the representative volume element (RVE) at the microscale. Works are also found in the field of biomechanics. For instance, [28] focused on building a multilevel approach between the mechanical tissue and the cells as dilute spherical inclusions. [29] modelled the macroscale mechanical behaviour of soft collagenous tissues by a 3-level multiscale description, from nanoscale up to the macroscale. [30] proposed error estimations for transferring information between the scales. Some research into multiscale and large strains is conducted in a number of works. However, they are using either a different numerical method, i.e not FEM, or they are performing the technique with a distinct strategy to the one presented here. Inside the first group, the work by [31] deals with large strains within a multiscale meshfree method framework. In the second group, i.e. [32] presented a multiscale approach at finite strains based on principles of energy minimization and by means of a global internal parameter description associated to the dissipation. In this paper, a new multiscale methodologogy is proposed. The technique is characterised by imposing antiperiodic tractions and periodic prescribed displacements at the boundary of the RVE leading to a particular condensation technique. Formulation including tangent modulus for an implicit solution as well as details of the solver employed are provided. The overall macroscopic deformation gradient $\overline{\mathbf{F}}$ is

*j.curiel-sosa@sheffield.ac.uk (JL Curiel-Sosa)

prescribed over the discretised RVE. This paper is organised as follows. Firstly, background, definitions and special boundary conditions imposed on the representative volume element (RVE) for the multiscale large strain methodology are introduced. Secondly, the proposed discretised multiscale model at large strains is presented with details of the solver algorithmic procedure. Finally, a number of numerical tests for distinct boundary conditions and variables in terms of void densities are presented before concluding.

2. Theoretical background

A homogenized macro-continuum, in its deformed configuration, with locally attached microstructures is considered 1. The microstructure $\mathbb{B} \subset \mathbb{R}^3$ is considered, with overall properties related to the macro-continuum $\overline{\mathbb{B}} \subset \mathbb{R}^3$. The *microscopic deformation gradient* is defined, following the general definition, by

$$\mathbf{F}_\mu(\mathbf{Y}, t) \equiv \frac{\partial\, \boldsymbol{\phi}}{\partial\, \mathbf{Y}} \equiv \frac{\partial\, \boldsymbol{y}}{\partial\, \mathbf{Y}} \equiv \nabla_0\, \boldsymbol{y} \tag{1}$$

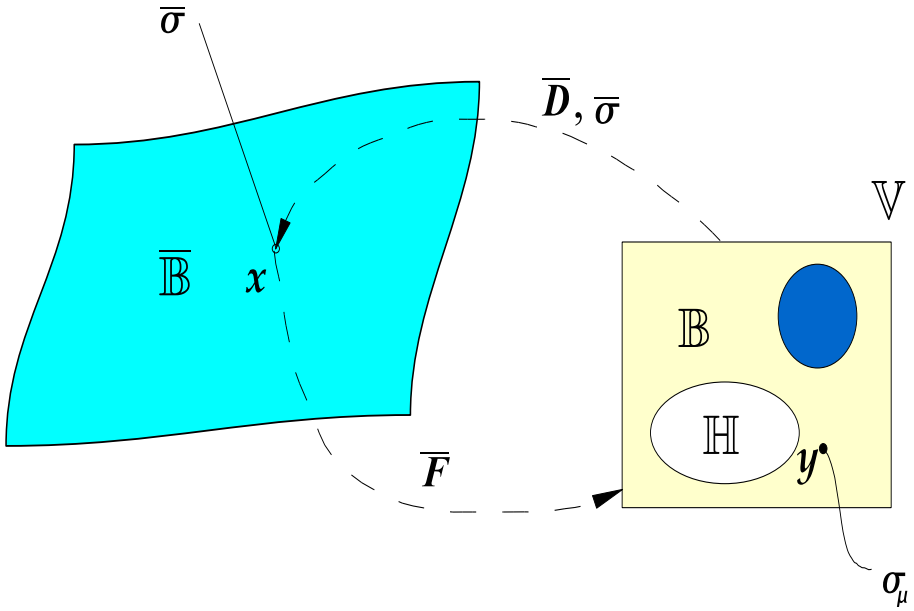

Figure 1: Micro to macro transition

where $\boldsymbol{y} \in \mathbb{B}$ is the spatial point, $\mathbb{B}$ is the spatial configuration of the microstructure, and $\boldsymbol{y} \in \mathbb{B}_0$ the corresponding material point of the microstructure in undeformed configuration $\mathbb{B}_0$. Therefore, the microscopic deformation gradient is defined as the material gradient of the spatial coordinates. The *microscopic small strain tensor* $\boldsymbol{\epsilon}_\mu$ is defined for the finite strain analysis as the symmetric part of the spatial displacement gradient tensor, i.e.

$$\boldsymbol{\epsilon}_\mu(\mathbf{Y}, t) \equiv \mathrm{sym}\{\nabla \mathbf{u}\} \equiv \frac{1}{2}\,[\,\nabla \mathbf{u} + (\nabla \mathbf{u})^{\mathrm{T}}] \tag{2}$$

where $\mathbf{u}$ is the displacement field at a material point $\boldsymbol{y} \in \mathbb{B}$. Microequilibrium state is assumed in its spatial form in the presence of body forces $\mathbf{b}$ per unit of mass,

$$\nabla \cdot \boldsymbol{\sigma}_\mu + \rho\, \mathbf{b} = \mathbf{0} \quad \text{in } \mathbb{B} \tag{3}$$

where $\boldsymbol{\sigma}_\mu$ is the symmetric microscopic Cauchy stress tensor. The material form of the equilibrium is given by (4).

$$\nabla_0 \cdot \mathbf{P}_\mu + \rho_0\, \mathbf{b} = \mathbf{0} \quad \text{in } \mathbb{B}_0 \tag{4}$$

The microscopic Kirchhoff symmetric stress tensor $\boldsymbol{\tau}_\mu$ is assumed to be related to the Cauchy stress tensor by $\boldsymbol{\tau}_\mu = J_\mu\, \boldsymbol{\sigma}_\mu$. A constitutive law is assumed to be given in the form $\boldsymbol{\tau}_\mu = \hat{\boldsymbol{\tau}}_\mu(\mathbf{F}_\mu\ ;\boldsymbol{\alpha}\ ;\ \boldsymbol{y})$ in $\mathbb{B}$. $\boldsymbol{\alpha}$ is a set of internal variables. The simplest example is elastic constitutive model is given in (5) with ψ denoting a strain energy function.

$$\boldsymbol{\tau}_\mu = \frac{\partial \psi(\boldsymbol{\tau}_\mu\ ;\ \boldsymbol{y})}{\partial \mathbf{F}_\mu} \quad \text{in } \mathbb{B} \tag{5}$$

Applying Gauss theorem in (3) the global microequilibrium condition are obtained

$$\int_{\partial\mathbb{B}} \mathbf{t}\ \mathrm{d}A + \int_{\mathbb{B}} \rho\, \mathbf{b}\ \mathrm{d}V = \mathbf{0} \quad \text{and} \quad \int_{\partial\mathbb{B}} \boldsymbol{y} \times \mathbf{t}\ \mathrm{d}A + \int_{\mathbb{B}} \boldsymbol{y} \times \rho\, \mathbf{b}\ \mathrm{d}V = \mathbf{0} \tag{6}$$

where $\mathbf{t} = \boldsymbol{\sigma}_\mu \cdot \mathbf{n}$ on $\partial\mathbb{B}$ denotes the traction field on the surface with outward normal $\mathbf{n}$ at $\boldsymbol{y} \in \partial\mathbb{B}$.

3. Macro-variables definitions

3.1. Overall deformation gradient

The macro deformation gradient $\mathbf{F}_\mathrm{M}$ is defined as an average over the undeformed unit cell and denoted by $\overline{\mathbf{F}}$. By applying Green's Lemma the following expression is obtained

$$\mathbf{F}_\mathrm{M} \equiv \overline{\mathbf{F}} = \frac{1}{|\mathbb{V}_0|} \int_{\partial\mathbb{V}_0} [\boldsymbol{y} \otimes \mathbf{N}]\ \mathrm{d}A_0 \tag{7}$$

in terms of the spatial coordinates at $\boldsymbol{y} \in \partial\mathbb{V}$ and the outward normal vector $\mathbf{N} \in \partial\mathbb{V}_0$.

3.2. Overall Kirchhoff macrostress

The macroscopic Kirchhoff stress tensor $\boldsymbol{\tau}_\mathrm{M}$ is defined in terms of the macroscopic average Cauchy stress tensor$\boldsymbol{\tau}_\mathrm{M} \equiv J_\mathrm{M}\, \boldsymbol{\sigma}_\mathrm{M} = J_\mathrm{M}\, \overline{\boldsymbol{\sigma}}$. Note that $\boldsymbol{\tau}_\mathrm{M}$ is equal to the average Kirchhoff stress tensor over the microstructure$\boldsymbol{\tau}_\mathrm{M} = \overline{\boldsymbol{\tau}}$. Thus, it is defined as follows,

$$\boldsymbol{\tau}_\mathrm{M} \equiv \overline{\boldsymbol{\tau}} \ = \ \frac{1}{|\mathbb{V}_0|} \int_{\partial\mathbb{V}} \mathrm{sym}[\mathbf{t} \otimes \boldsymbol{y}]\ \mathrm{d}A + \ \frac{1}{|\mathbb{V}_0|} \int_{\mathbb{V}} \rho\ \mathrm{sym}[\mathbf{b} \otimes \boldsymbol{y}]\ \mathrm{d}V \tag{8}$$

3.3. Overall spatial tangent modulus

The modulus $\overline{\boldsymbol{\mathcal{D}}}^{\tau \mathrm{F}}$, in a general continuum form, relates the variations of the overall macro Kirchhoff stress $\overline{\boldsymbol{\tau}}$ and the macro-deformation gradient tensor $\overline{\mathbf{F}}$ in the following form

$$\overline{\boldsymbol{\mathcal{D}}}^{\tau \mathrm{F}} \equiv \frac{\partial \overline{\boldsymbol{\tau}}}{\partial \overline{\mathbf{F}}} \tag{9}$$

Overall spatial tangent modulus $\overline{\boldsymbol{\mathcal{A}}}$ is expressed as follows,

$$\overline{\boldsymbol{\mathcal{A}}} = \frac{1}{J} \overline{\boldsymbol{\mathcal{D}}}^{\tau \mathrm{F}} \diamond \overline{\mathbf{F}} - \overline{\boldsymbol{\sigma}} \star \mathbf{I} \tag{10}$$

$$\overline{A}_{ijkl} = \frac{1}{J} \frac{\partial \overline{\tau}_{ij}}{\partial \overline{F}_{km}} \overline{F}_{lk} - \overline{\sigma}_{il} \delta_{jk} \tag{11}$$

4. Boundary conditions at the microscale

The boundary conditions for the displacement $\mathbf{u}$ and traction $\mathbf{t}$ on the microstructure, are chosen such that the Hill-Mandel Principle [33] is satisfied. Boundary conditions are prescribed on the unit cell as follows: (a) Taylor assumption, (b) linear displacements on the boundary and (c) periodic displacements and antiperiodic traction on the boundary. Being the latter one the focus of this study and, hence, detailed description is provided for it. A crucial aspect of our approach is the formulation on a deformation-driven context, where the macroscopic deformation gradient $\overline{\mathbf{F}}$ is prescribed. The spatial coordinate field is divided in two parts

$$\boldsymbol{y}(\mathbf{Y}) = \mathbf{y}^*(\mathbf{Y}) + \tilde{\mathbf{u}}(\mathbf{Y}) = \overline{\mathbf{F}}\,\mathbf{Y} + \tilde{\mathbf{u}}(\mathbf{Y}) \tag{12}$$

where $\mathbf{y}^*$ is the *Taylor spatial coordinate*, which defines a constant deformation gradient $\overline{\mathbf{F}}$ over the unit cell as $\mathbf{y}^* \equiv \overline{\mathbf{F}}\,\mathbf{Y}$. $\tilde{\mathbf{u}}$ is the *displacement fluctuation*, which is considered to be the unknown. Using the averaging theorem by [33] yields,

$$\frac{1}{|\mathbb{V}_0|} \int_{\partial \mathbb{V}_0} \mathbf{t}_0 \cdot \tilde{\mathbf{u}} \, \mathrm{d}A_0 + \frac{1}{|\mathbb{V}_0|} \int_{\mathbb{V}} \rho_0 \, \mathbf{b} \cdot \tilde{\mathbf{u}} \, \mathrm{d}V_0 = 0 \tag{13}$$

4.1. Periodic deformation and antiperiodic traction on the boundary of RVE in large strain

Another possibility consists of applying periodic deformation and antiperiodic traction on the boundary of the RVE $\partial \mathbb{V}$, which is represented as

$$\boldsymbol{y}(\mathbf{Y}^+) - \boldsymbol{y}(\mathbf{Y}^-) = \overline{\mathbf{F}}\,(\mathbf{Y}^+ - \mathbf{Y}^-) \tag{14}$$

$$\mathbf{t}(\mathbf{Y}^+) = -\mathbf{t}(\mathbf{Y}^-) \tag{15}$$

By taking into consideration the displacement field division (12), the periodic deformation condition above (14) can also be imposed by enforcing the displacement fluctuation on the boundary of RVE to be periodic, hence

$$\widetilde{\mathbf{u}}(\mathbf{Y}^{+}) \;=\; \widetilde{\mathbf{u}}(\mathbf{Y}^{-}) \tag{16}$$

In order to apply these conditions the boundary of the unit cell is decomposed in two parts as indicated in Figure 2. Thus $\partial\mathbb{V} = \partial\mathbb{V}^{+} \cup \partial\mathbb{V}^{-}$ with outwards normals $\mathbf{n}^{+} = -\mathbf{n}^{-}$ which are associated with the points $\boldsymbol{y}^{+} \in \partial\mathbb{V}^{+}$ and $\boldsymbol{y}^{-} \in \partial\mathbb{V}^{-}$.

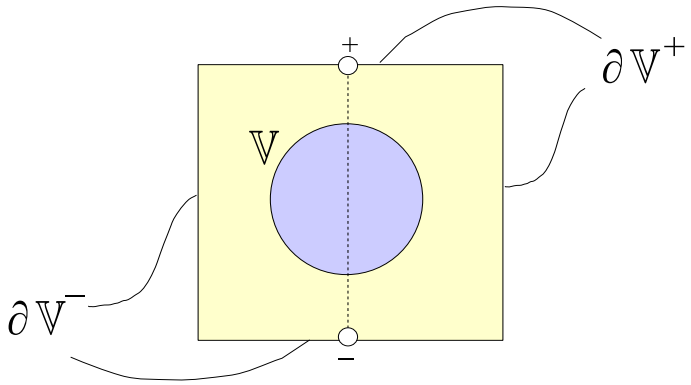

Figure 2: Microstructure for periodic b.c.

Body force is not taken into consideration so that this condition satisfy the averaging theorem. This is proved easily by inserting the periodic displacement fluctuation (16) and antiperiodic traction (15) into the form of the averaging theorem (13).

5. Multiscale discretised model at large strains

RVE microstructure is considered as representation of the macro Gauss point. Based on the F.E. discretisation of the microstructure, a procedure for computing the overall tangent modulus $\overline{\boldsymbol{\mathcal{A}}}$ and macroscopic average Kirchhoff stress $\overline{\boldsymbol{\tau}}$ (or Cauchy $\overline{\boldsymbol{\sigma}}$) at each macroscopic integration point with locally attached microstructure is developed. The spatial coordinate field is divided in two parts,

$$\mathbf{y} \;= \mathbf{y}^{*} + \widetilde{\mathbf{u}} \tag{17}$$

where the *Taylor spatial coordinate* $\mathbf{y}^{*}$ is expressed in its discrete form as,

$$\mathbf{y}^{*}_{\mathrm{j}} \;\equiv\; \overline{\mathbf{F}}\,\mathbf{Y}_{\mathrm{j}} \quad \mathrm{j} \;=\; 1 \cdots \mathrm{n} \tag{18}$$

for the n nodes of the microstructure RVE. The *displacement fluctuation* $\widetilde{\mathbf{u}}$ is the unknown for every node of the discretised microstructure unit cell.

$$\overline{\mathbf{F}} \;\equiv\; \left\{ \begin{array}{c} \overline{F}_{11} \\ \overline{F}_{21} \\ \overline{F}_{12} \\ \overline{F}_{22} \end{array} \right\} \quad \text{and} \quad \mathbf{u}_{\mathrm{j}} \;\equiv\; \left\{ \begin{array}{c} u_1 \\ u_2 \end{array} \right\}_{\mathrm{j}} \tag{19}$$

with $\overline{\mathbf{F}}$ being matrix representation of macro-deformation gradient tensor and $\mathbf{u}_\mathrm{j}$ the displacement field at node j of the discretised unit cell $\mathbb{V}$.

The *Taylor coordinate* $\mathbf{y}_\mathrm{j}^*$ of the node j is computed in the following matrix form

$$\mathbf{y}_\mathrm{j}^* \;=\; \mathbb{D}_{0\mathrm{j}}^{\mathrm{T}}\,\overline{\mathbf{F}} \quad \mathrm{j} \;=\; 1 \cdots \mathrm{n}. \tag{20}$$

where $\mathbb{D}_{0\mathrm{j}}$ is the *material coordinate matrix* at node j of the microstructure

$$\mathbb{D}_{0\mathrm{j}} \;\equiv\; \begin{bmatrix} Y_1 & 0 \\ 0 & Y_1 \\ Y_2 & 0 \\ 0 & Y_2 \end{bmatrix}_\mathrm{j} \tag{21}$$

6. Large strains microstructure equilibrium solution

An iteration determines the current fluctuation field via the update

$$\mathbf{u} \;\leftarrow \widetilde{\mathbf{u}} + \delta\widetilde{\mathbf{u}} \tag{22}$$

It is assumed that the microstructure RVE, corresponding to a macroscopic Gauss point has reached equilibrium at time step n. The goal is to compute equilibrium at the time step $n+1$ with the incremental strain $\triangle\overline{\mathbf{F}}$ information passed from the macroscale from the global iteration to the microscale RVE. From the multiplicative nature of the deformation gradient follows that

$$\overline{\mathbf{F}}_{n+1} = \triangle\overline{\mathbf{F}} \cdot \overline{\mathbf{F}}_n \tag{23}$$

The incremental boundary value problem for the microstructure RVE is established as follows:

Given: The displacement field $\mathbf{u}_n$, the Cauchy stress field $\boldsymbol{\sigma}_n$ and the set of internal variables $\boldsymbol{\alpha}_n$ at time step n and the incremental macro deformation gradient $\triangle\overline{\mathbf{F}}$.

Find: The displacement field $\mathbf{u}_{n+1}$, the Cauchy stress field $\boldsymbol{\sigma}_{n+1}$ and the set of internal variables $\boldsymbol{\alpha}_{n+1}$ at time step $n+1$. In addition, the macroscopic Kirchhoff stress $\overline{\boldsymbol{\tau}}_{n+1}$ is computed, once the microstructure is in equilibrium using (36). The macro Cauchy stress $\overline{\boldsymbol{\sigma}}_{n+1}$ is immediately deduced as,

$$\overline{\boldsymbol{\sigma}}_{n+1} = \frac{1}{J_{n+1}}\,\overline{\boldsymbol{\tau}}_{n+1} \tag{24}$$

where $J_{n+1} = \det(\overline{\mathbf{F}}_{n+1})$. The macro Cauchy stress $\overline{\boldsymbol{\sigma}}_{n+1}$ is returned back to the macroscale and used as a macrostress at macro Gauss point level corresponding to the microstructure RVE computed. The procedure differs depending on the boundary constraint applied over the microstructure RVE. Note that the incremental displacement field, $\triangle\mathbf{u} = \mathbf{u}_{n+1} - \mathbf{u}_n = \triangle\mathbf{y} = \mathbf{y}_{n+1} - \mathbf{y}_n$is additively decomposed as,

$$\triangle\mathbf{u} = \triangle\mathbf{u}^* + \widetilde{\mathbf{u}}_{n+1} \tag{25}$$

where the notation $\triangle \mathbf{u}^*$ is used for

$$\triangle \mathbf{u}^* = \mathbf{y}^*_{n+1} - \mathbf{y}_n = \overline{\mathbf{F}}_{n+1}\mathbf{Y} - \mathbf{y}_n. \tag{26}$$

The sequence of the solution procedure is,

1. The initial incremental displacement $\triangle \mathbf{u}^0$,

$$\triangle \mathbf{u}^0 = \triangle \mathbf{u}^* + \widetilde{\mathbf{u}}_n \tag{27}$$

$$\mathbf{y}^0_{n+1} = \mathbf{y}_n + \triangle \mathbf{u}^0 \tag{28}$$

$$\mathbf{y}^0_{n+1} = \mathbf{y}^*_{n+1} + \widetilde{\mathbf{u}}_n \tag{29}$$

$$\widetilde{\mathbf{u}}^0_{n+1} = \widetilde{\mathbf{u}}_n \tag{30}$$

2. Computation of the internal forces $\mathbf{f}^{int}$. This is computed with the incremental displacement $\triangle \mathbf{u}$ and the set of state variables $\{\mathbf{F}_{n+1}, \boldsymbol{\alpha}_{n+1}\}$ at microscopic Gauss point level.
3. Check convergence
   - if $\|\mathbf{r}\| < \varepsilon_{tolerance}$, the solution is $\mathbf{u}^k_{n+1}$, then iterations end;
   - else go to next step
4. Computation of the incremental internal fluctuation,

$$\delta\widetilde{\mathbf{u}} = \left\{ \begin{array}{c} \delta\widetilde{\mathbf{u}}_r \\ \delta\widetilde{\mathbf{u}}_d \end{array} \right\} \tag{31}$$

The Newton-Raphson iteration is defined by,

$$\mathbf{K}_r \; \delta\widetilde{\mathbf{u}}_r = -\mathbf{r} \quad \rightarrow \quad \delta\widetilde{\mathbf{u}}_r = -\mathbf{K}_r^{-1} \; \mathbf{r} \tag{32}$$

The updating,

$$\triangle\widetilde{\mathbf{u}} \; \leftarrow \triangle\widetilde{\mathbf{u}} + \delta\widetilde{\mathbf{u}} \tag{33}$$

$$\triangle\mathbf{u} \; \leftarrow \triangle\mathbf{u} + \delta\widetilde{\mathbf{u}} \tag{34}$$

Go to step 2.

Finally, when the microequilibrium is reached, the macro Kirchhoff stress $\overline{\boldsymbol{\tau}}_{n+1}$ is computed from the value of the boundary forces. Then, the macro Cauchy stress (24) is used for computing the internal forces at the macro level.

7. General average Kirchhoff stress and overall spatial tangent modulus computation

Assuming no body forces in the expression for the average Kirchhoff stress (8), in the discrete setting, $\mathbf{t}\ \mathrm{d}A \to \boldsymbol{f}_{\mathrm{j}}^{ext}$, that is the infinitesimal force $\mathbf{t}\ \mathrm{d}A$ becomes the finite force $\boldsymbol{f}_{\mathrm{j}}^{ext}$ at nodal position $\mathbf{y}_{\mathrm{j}}$ on the boundary $\partial\mathbb{V}$. Therefore (8) degenerates into the discrete sum

$$\overline{\boldsymbol{\tau}} \ = \frac{1}{|\mathbb{V}_0|} \sum_{\mathrm{j}\ =\ 1}^{\mathrm{n_b}} \mathrm{sym}[\boldsymbol{f}_{\mathrm{j}}^{ext} \otimes \mathbf{y}_{\mathrm{j}}] \tag{35}$$

where $\mathrm{n_b}$ is the number of nodes on the boundary $\partial\mathbb{V}$. Using matrix representation this expression becomes,

$$\overline{\boldsymbol{\tau}} \ = \frac{1}{|\mathbb{V}_0|} \sum_{\mathrm{j}\ =\ 1}^{\mathrm{n_b}} \mathbb{D}_{\mathrm{j}}\ \boldsymbol{f}_{\mathrm{j}}^{ext} \tag{36}$$

where $\mathbb{D}_{\mathrm{j}}$ is the *spatial coordinate matrix* evaluated at node j on the boundary of the discretised microstructure RVE

$$\mathbb{D}_{\mathrm{j}} \ \equiv \ \frac{1}{2} \begin{bmatrix} 2\,y_1 & 0 \\ 0 & 2\,y_2 \\ y_2 & y_1 \end{bmatrix}_{\mathrm{j}} \tag{37}$$

The above expression is rearranged in the following global expression

$$\overline{\boldsymbol{\tau}} \ = \ \frac{1}{|\mathbb{V}_0|}\ \mathbb{D}_{\mathrm{b}}\ \mathbf{f}_{\mathrm{b}}^{ext}\ , \tag{38}$$

where $\mathbf{f}_{\mathrm{b}}^{ext}$ is the external nodal force vector of the boundary nodes, and $\mathbb{D}_{\mathrm{b}}$ is the *boundary coordinate matrix* defined by $\mathbb{D}_{\mathrm{b}} \ \equiv \left[\ \mathbb{D}_1^b \quad \mathbb{D}_2^b \quad \ldots \quad \mathbb{D}_{\mathrm{n_b}}^b\ \right]$

7.1. Overall spatial tangent modulus computation for large strains

In the computational homogenization approach no explicit form of the constitutive behavior on the macro-level is assumed a priori, the tangent modulus is determined numerically by relations between variations of the macroscopic stress and variations of the macroscopic strain at such integration macro Gauss point. This is accomplished by numerical differentiation of the numerical macroscopic stress-strain relation, for instance, by using forward difference approximations as suggested in [34]. Another approach is to condense the microstructural stiffness matrix to the macroscopic matrix tangent modulus. This task is achieved by reducing the total RVE system of equations to the relation between the forces acting on the boundary $\partial\mathbb{V}$ and the displacement on the boundary. We propose a direct condensation to obtain a relation between the variation of the forces acting on the boundary $\partial\mathbb{V}$ and the variational Taylor spatial coordinate on the boundary nodes array $\mathrm{d}\mathbf{y}^*$ which depends linearly of the macroscopic deformation variation $\mathrm{d}\overline{\mathbf{F}}$ as described below. The total microstructural system of equations that gives the relation between the iterative nodal displacement $\mathrm{d}\mathbf{u}$ and iterative nodal external force vectors is,

$$\mathbf{K}\ \mathrm{d}\mathbf{u} = \mathrm{d}\mathbf{f}^{ext}. \tag{39}$$

Due to $\mathrm{d}\mathbf{y} = \mathrm{d}\mathbf{u}$ and the spatial coordinate partition (17) we have the following differential relation,

$$\mathrm{d}\mathbf{u} = \mathrm{d}\mathbf{y}^* + \mathrm{d}\widetilde{\mathbf{u}} \tag{40}$$

The system (39) is rearranged as follows

$$\mathbf{K}\ \mathrm{d}\mathbf{u} = \mathrm{d}\mathbf{f}^{ext}\ \Rightarrow\ \mathbf{K}\ (\mathrm{d}\mathbf{y}^* + \mathrm{d}\widetilde{\mathbf{u}}) = \mathrm{d}\mathbf{f}^{ext}\ \Rightarrow \tag{41}$$

$$\mathbf{K}\ \mathrm{d}\mathbf{y}^* + \mathbf{K}\ \mathrm{d}\widetilde{\mathbf{u}} = \mathrm{d}\mathbf{f}^{ext} \tag{42}$$

The boundary constraints are then applied to this system in the following sections to condense the system. This procedure gives the expression that relates the variation of boundary external forces $\mathrm{d}\mathbf{f}_{\mathrm{b}}^{ext}$ against the variation of the Taylor spatial coordinate $\mathrm{d}\mathbf{y}^*$. The overall modulus $\overline{\boldsymbol{\mathcal{D}}}^{\tau\mathrm{F}}$ defined in (9)is computed in its discretised F.E. matrix form, using averaged Kirchhoff stress expression (38), as follows

$$\overline{\boldsymbol{\mathcal{D}}}^{\tau\mathrm{F}}\ =\ \frac{\mathrm{d}\overline{\boldsymbol{\tau}}}{\mathrm{d}\overline{\mathbf{F}}}\ =\ \frac{1}{|\mathbb{V}_0|}\,\mathbb{D}_{\mathrm{b}}\,\frac{\mathrm{d}\mathbf{f}_{\mathrm{b}}^{ext}}{\mathrm{d}\overline{\mathbf{F}}} \tag{43}$$

The overall spatial tangent modulus (10) is computed in its matrix form for heterogeneous material with different microstructures as,

$$\overline{\boldsymbol{\mathcal{A}}} = \frac{1}{J}\overline{\boldsymbol{\mathcal{D}}}^{\tau\mathrm{F}} \diamond \overline{\mathbf{F}} - \overline{\boldsymbol{\sigma}} \star \mathbf{I}. \tag{44}$$

This matrix form is obtained by converting the continuous form (11) to the matrix form used in the discrete formulation. Particularisations of the computation average Kirchhoff macrostress and overall spatial tangent modulus are given in the following subsections of this section, for Taylor assumption, linear b.c. and periodic b.c.

8. Periodic displacements and antiperiodic traction on the boundary of RVE discrete in large strain

In order to discretise the continuum model of the periodic boundary conditions described in Section 4.1, the nodes of the mesh are partitioned in four groups as follows,

1. $\mathrm{n_i}$ interior nodes are distinguished.
2. $\mathrm{n_p}$ positive boundary nodes which are located at the top and right side of the microstructure surface $\partial\mathbb{V}$ of RVE.
3. $\mathrm{n_p}$ negative boundary nodes which are located at the bottom and left side of the microstructure surface $\partial\mathbb{V}$ of RVE.
4. $\mathrm{n_c}$ node at the corners.

The number of node pairs (positive and corresponding negative nodes) on the boundary $\partial\mathbb{V}$ of RVE are:

$$\mathrm{n_p}\ =\ \frac{\mathrm{n_b}}{2}\ -\ 2 \tag{45}$$

where n_b is the total number of nodes on the boundary of RVE. Also the number of corner nodes in a 2D rectangular microstructure is four, $n_c = 4$

9. Periodic displacements and antiperiodic traction discrete b.c.

At each node pair j on the boundary $\partial\mathbb{V}^+ \cup \partial\mathbb{V}^-$, the continuum condition (16) induces the discrete constraint $\widetilde{\mathbf{u}}_j^+ = \widetilde{\mathbf{u}}_j^- , \quad j = 1 \cdots n_p$. The link between constraints for each pair of nodes is compactly represented in a global form as $\widetilde{\mathbf{u}}_p = \widetilde{\mathbf{u}}_n$. The displacement fluctuation at the corners is prescribed to zero to avoid the rigid body motion, i.e.

$$\widetilde{\mathbf{u}}_{ci} = \mathbf{0} , \qquad i = 1 \cdots n_c \tag{46}$$

Note that (46) agrees with the periodic continuum condition (16). The relation (46) is represented in a global form $\widetilde{\mathbf{u}}_c = \mathbf{0}$. At each node pair j on the boundary $\partial\mathbb{V}^+ \cup \partial\mathbb{V}^-$, the continuum antiperiodic traction condition (15) is discretised as

$$\mathbf{f}(\mathbf{y}_j^+) = -\mathbf{f}(\mathbf{y}_j^-) \ \text{ or } \ \mathbf{f}_j^+ = -\mathbf{f}_j^- , \qquad j = 1 \cdots n_p \tag{47}$$

Again these constraints, are represented in compressed form as $\mathbf{f}_p^{ext} = -\mathbf{f}_n^{ext}$. An important additional equation to take into consideration is equilibrium condition given by

$$\sum_{i=1}^{4} \mathbf{f}_{ci}^{ext} = \mathbf{0} \tag{48}$$

Note that this equation agrees with the continuum antiperiodic traction condition (15). The underlying idea relies on the antiperiodicity of force in the corners that come from the different continuum distributions. Using the matrix notation, we redefine the *global material coordinate matrix* for periodic b.c. as $\mathbb{D}_{0\text{global},p} \equiv \begin{bmatrix} \mathbb{D}_{0i} & \mathbb{D}_{0b,p} \end{bmatrix}$ where $\mathbb{D}_{0i}$ is the *interior material coordinate matrix* and the $\mathbb{D}_{0b,p}$ and is the *boundary material coordinate matrix* for Periodic b.c. defined as $\mathbb{D}_{0b,p} = \begin{bmatrix} \mathbb{D}_{0p} & \mathbb{D}_{0n} & \mathbb{D}_{0c} \end{bmatrix}$ where $\mathbb{D}_{0p}$, $\mathbb{D}_{0n}$ and $\mathbb{D}_{0c}$ are the *positive boundary material coordinate matrix*, *negative boundary material coordinate matrix* and *corner material coordinate matrix*, respectively.

The Taylor spatial coordinate $\mathbf{y}^*$ defined as a constant for each node in (20), is given in a compact form as $\mathbf{y}^* = \mathbb{D}_{0\text{global},p}^{\mathrm{T}} \overline{\mathbf{F}}$ where $\mathbb{D}_{0\text{global},p}$ is the global material coordinate matrix for Periodic b.c. and $\overline{\mathbf{F}}$ is the matrix representation of the prescribed macroscopic deformation gradient tensor. In this model the variation of the Taylor spatial coordinate vector $\mathrm{d}\mathbf{y}^*$ is considered as follows

$$\mathrm{d}\mathbf{y}^* = \mathbb{D}_{0\text{global},p}^{\mathrm{T}} \, \mathrm{d}\overline{\mathbf{F}} , \tag{49}$$

Note that the variation of the coordinate $\mathrm{d}\mathbf{y}^*$ is a function of the variation of the macroscopic average deformation gradient vector $\mathrm{d}\overline{\mathbf{F}}$.

9.1. Average Kirchhoff macro-stress for the anti–periodic b.c.

Following the procedure to compute average stress given in Section (7), the average Kirchhoff stress is computed based on (36) as follows,

$$\overline{\boldsymbol{\tau}} = \frac{1}{|\mathbb{V}_0|} \left[\sum_{\mathrm{j}\,=\,1}^{\mathrm{n_p}} (\mathbb{D}_{\mathrm{j}}^{+} - \mathbb{D}_{\mathrm{j}}^{-}) \, \mathbf{f}_{\mathrm{j}}^{+ext} + \sum_{\mathrm{i}\,=\,1}^{4} \mathbb{D}_{ci} \, \mathbf{f}_{\mathrm{ci}}^{ext} \right] \tag{50}$$

We define the *boundary spatial coordinate matrix* $\mathbb{D}_{\mathrm{b},p}$ as

$$\mathbb{D}_{\mathrm{b},p} = \left[\mathbb{D}_{\mathrm{p}} \quad \mathbb{D}_{\mathrm{n}} \quad \mathbb{D}_{\mathrm{c}} \right] \tag{51}$$

where $\mathbb{D}_{\mathrm{p}}$, $\mathbb{D}_{\mathrm{n}}$ and $\mathbb{D}_{\mathrm{c}}$ are the *positive boundary spatial coordinate matrix*, *negative boundary spatial coordinate matrix* and *corner spatial coordinate matrix*

Then, the expression for the averaged Kirchhoff stress (50) in a global form is given by

$$\overline{\boldsymbol{\tau}} = \frac{1}{|\mathbb{V}_0|} \, \mathbb{D}_{\mathrm{b},p} \, \mathbf{f}_{\mathrm{b}}^{ext} \tag{52}$$

where global matrix notation is used. Note that $\mathbf{f}_{\mathrm{b}}^{ext}$ is the external boundary force vector which is obtained by gathering operation of the external force vector to extract the positive $\mathbf{f}_{\mathrm{p}}^{ext}$, negative $\mathbf{f}_{\mathrm{n}}^{ext}$ and corner $\mathbf{f}_{\mathrm{c}}^{ext}$ counterpart in the expression

$$\mathbf{f}_{\mathrm{b}}^{ext} = \left\{ \begin{array}{c} \mathbf{f}_{\mathrm{p}}^{ext} \\ \mathbf{f}_{\mathrm{n}}^{ext} \\ \mathbf{f}_{\mathrm{c}}^{ext} \end{array} \right\}$$

9.2. Overall spatial tangent modulus for the anti–periodic b.c.

After gathering and rearranging the displacement nodal vector $\mathbf{u}$, the external nodal force vector $\mathbf{f}^{ext}$ and finally the stiffness matrix $\mathbf{K}$, the general system (39) that relates the variations $\mathrm{d}\mathbf{u}$ and $\mathrm{d}\mathbf{f}^{ext}$ is rearranged as follows

$$\begin{bmatrix} \mathbf{k}_{\mathrm{ii}} & \mathbf{k}_{\mathrm{ip}} & \mathbf{k}_{\mathrm{in}} & \mathbf{k}_{\mathrm{ic}} \\ \mathbf{k}_{\mathrm{pi}} & \mathbf{k}_{\mathrm{pp}} & \mathbf{k}_{\mathrm{pn}} & \mathbf{k}_{\mathrm{pc}} \\ \mathbf{k}_{\mathrm{ni}} & \mathbf{k}_{\mathrm{np}} & \mathbf{k}_{\mathrm{nn}} & \mathbf{k}_{\mathrm{nc}} \\ \mathbf{k}_{\mathrm{ci}} & \mathbf{k}_{\mathrm{cp}} & \mathbf{k}_{\mathrm{cn}} & \mathbf{k}_{\mathrm{cc}} \end{bmatrix} \begin{Bmatrix} \mathrm{d}\mathbf{u}_{\mathrm{i}} \\ \mathrm{d}\mathbf{u}_{\mathrm{p}} \\ \mathrm{d}\mathbf{u}_{\mathrm{n}} \\ \mathrm{d}\mathbf{u}_{\mathrm{c}} \end{Bmatrix} = \begin{Bmatrix} \mathrm{d}\mathbf{f}_{\mathrm{i}}^{ext} \\ \mathrm{d}\mathbf{f}_{\mathrm{p}}^{ext} \\ \mathrm{d}\mathbf{f}_{\mathrm{n}}^{ext} \\ \mathrm{d}\mathbf{f}_{\mathrm{c}}^{ext} \end{Bmatrix} \quad \equiv \quad \mathbf{K} \, \mathrm{d}\mathbf{u} = \mathrm{d}\mathbf{f}^{ext} \tag{53}$$

where $\mathrm{d}\mathbf{f}_{\mathrm{i}}^{ext} = \mathbf{0}$ in equilibrium. Splitting the spatial coordinate vector (17) and rearranging the system (53), leads to

$$\mathbf{K} \, \mathrm{d}\widetilde{\mathbf{u}} = \mathrm{d}\mathbf{f}^{ext} - \mathbf{K} \, \mathrm{d}\mathbf{y}^{*} \tag{54}$$

where the variation of Taylor coordinate $\mathrm{d}\mathbf{y}^{*}$ is given by (49). Then, the following expression is obtained,

$$\mathrm{d}\mathbf{f}_{\mathrm{b}}^{ext} \equiv \left\{ \begin{array}{c} \mathrm{d}\mathbf{f}_{\mathrm{p}}^{ext} \\ \mathrm{d}\mathbf{f}_{\mathrm{n}}^{ext} \\ \mathrm{d}\mathbf{f}_{\mathrm{c}}^{ext} \end{array} \right\} = \begin{bmatrix} \mathbf{K}^{\mathrm{P}} \\ -\mathbf{K}^{\mathrm{P}} \\ \hat{\mathbf{K}}^{\mathrm{C}} \end{bmatrix} \mathrm{d}\mathbf{y}^{*} = \mathbf{K}_{\mathbf{per}}^{\mathbf{B}} \, \mathrm{d}\mathbf{y}^{*} \tag{55}$$

This gives the expression

$$\mathrm{d}\mathbf{f}_{\mathrm{b}}^{ext} = \mathbf{K}_{\mathbf{per}}^{\mathbf{B}} \ \mathbb{D}_{0\mathrm{global},p}^{\mathrm{T}} \, \mathrm{d}\overline{\mathbf{F}} \tag{56}$$

where the Taylor coordinate variation (49) was inserted into the equation (55). Therefore, the desired expression is obtained as

$$\frac{\mathrm{d}\mathbf{f}_{\mathrm{b}}^{ext}}{\mathrm{d}\overline{\mathbf{F}}} = \mathbf{K}_{\mathbf{per}}^{\mathbf{B}} \ \mathbb{D}_{0\mathrm{global},p}^{\mathrm{T}} \tag{57}$$

which expresses the variation of the external boundary force vector $\mathrm{d}\mathbf{f}_{\mathrm{b}}^{ext}$ with respect to the variation of macroscopic average deformation gradient matrix $\mathrm{d}\overline{\mathbf{F}}$.

The overall modulus defined in (9)is computed in its discretised F.E. matrix form, using previous averaged stress expression (52), in the following way

$$\overline{\boldsymbol{\mathcal{D}}}_{p}^{\tau\mathrm{F}} = \frac{\mathrm{d}\overline{\boldsymbol{\tau}}}{\mathrm{d}\overline{\mathbf{F}}} = \frac{1}{|\mathbb{V}_0|} \, \mathbb{D}_{\mathrm{b},p} \, \frac{\mathrm{d}\mathbf{f}_{\mathrm{b}}^{ext}}{\mathrm{d}\overline{\mathbf{F}}} \tag{58}$$

where $\mathbb{D}_{\mathrm{b},p}$ was defined in (51).

Inserting (57) into (58), the matrix representation of $\overline{\boldsymbol{\mathcal{D}}}_{p}^{\tau\mathrm{F}}$ modulus is obtained as

$$\boxed{\overline{\boldsymbol{\mathcal{D}}}_{p}^{\tau\mathrm{F}} = \frac{1}{|\mathbb{V}_0|} \, \mathbb{D}_{\mathrm{b},p} \, \mathbf{K}_{\mathbf{per}}^{\mathbf{B}} \, \mathbb{D}_{0\mathrm{global},p}^{\mathrm{T}}} \tag{59}$$

Clearly, the modulus $\overline{\boldsymbol{\mathcal{D}}}_{p}^{\tau\mathrm{F}}$ is a function of the boundary spatial coordinate matrix $\mathbb{D}_{\mathrm{b},p}$ defined in (51), the condensed periodic stiffness matrix $\mathbf{K}_{\mathbf{per}}^{\mathbf{B}}$ and the global material coordinate matrix $\mathbb{D}_{0\mathrm{global},p}^{\mathrm{T}}$. The final step consists in inserting (59) into (44) to obtain

$$\overline{\boldsymbol{\mathcal{A}}}_{p} = \frac{1}{J} \overline{\boldsymbol{\mathcal{D}}}_{p}^{\tau\mathrm{F}} \diamond \overline{\mathbf{F}} - \overline{\boldsymbol{\sigma}} \star \mathbf{I} \tag{60}$$

which represents the overall spatial tangent modulus for anti–periodic b.c. in the matrix form. Finally, we remark that with the above expression (60), the tangent modulus is computed for heterogeneous material with different microstructures RVE gaining the desired *quadratic rate of convergence* for the Newton-Raphson solution procedure applied to solve the homogenized nonlinear macrostructure, under *periodic deformation* and *antiperiodic traction* on the boundary of RVE model.

10. Internally pressurised hyperelastic cylinder subjected to large strains

This section describes the simulation of an internally pressurised cylinder (internal radius $a = 0.1\,m$ and external radius $0.2\,m$) made of nonlinear material with microvoids of different shapes subjected to large strains. The analysis is carried out assuming *plane strain* conditions and a Neo-Hookean material model. Due to symmetry, only a quarter of the cylinder is considered, and discretized by 20 standard 8-nodes quadrilateral elements. The pressure, P, is prescribed on the inner surface, and it is increased gradually. The properties of the material are: logarithmic bulk modulus K = 2.667 GPa and shear modulus G = 0.889 GPa.

10.1. Internal pressure vs outer surface displacement diagrams

In the following figures, diagrams showing the applied pressure P versus radial displacement at the outer face of the plate are plotted as described earlier. The following diagrams are displayed:

- Single scale FEM analysis, **i.e. referring to the simulation considering no distinct scales with an elastic-plastic material model** .
- Two scale analysis. RVE: Square microstructure discretised by 8-noded quadrilateral elements with reduced integration. Every cell has a void in the middle with variable shape and volume fraction:
  - Microstructure 1: Circular void in the middle of RVE with 5 % volume fraction. $\mathrm{n}_{elements} = 126$, $\mathrm{n}_{nodes} = 438$.
  - Microstructure 2: Square void in the middle of RVE with 5 % volume fraction. $\mathrm{n}_{elements} = 128$, $\mathrm{n}_{nodes} = 448$.
  - Microstructure 3: Circular void in the middle of RVE with 15 % volume fraction. $\mathrm{n}_{elements} = 128$, $\mathrm{n}_{nodes} = 448$.
  - Microstructure 4: Square void in the middle of RVE with 15 % volume fraction. $\mathrm{n}_{elements} = 160$, $\mathrm{n}_{nodes} = 560$.

These Microstructures are depicted in Figure 3.

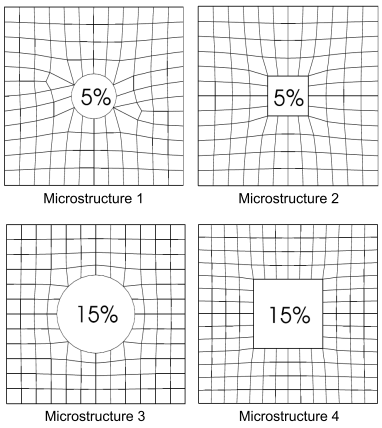

Figure 3: Microstructures for analysis of internally pressurised hyperelastic cylinder

In Figures 4 and 5 results are shown for different constraints on the microcell and 5 and 15% void fraction, respectively. A full curve shows finite element (FE) single scale analysis. Two scales results are depicted for Taylor assumption, linear b.c and periodic b.c. The results are as follows:

- Taylor assumption gives the stiffest response.
- For each microstructure linear b.c. shows a slightly stiffer response than periodic.
- **There are no significant differences associated to these distinct boundary conditions.**

The following diagrams 6, 7 and 8 show respectively how the result vary for each constraint, Taylor assumption, linear b.c. an periodic b.c., with the void volume fraction. It is observed clearly that the material response softens when the void volume fraction increases. The Taylor assumption shows less sensitive results than linear b.c. and periodic b.c.

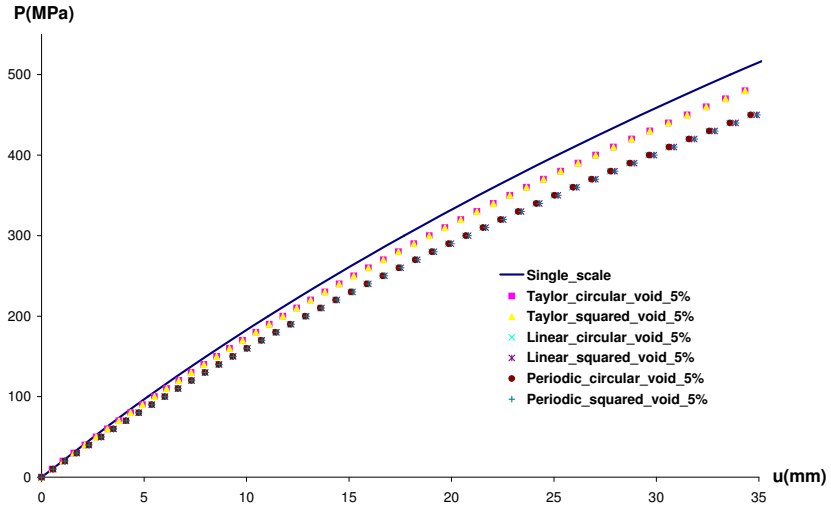

Figure 4: Internally pressurised hyperelastic cylinder. Pressure vs displacement diagram for full material and void at 5% volume fraction.

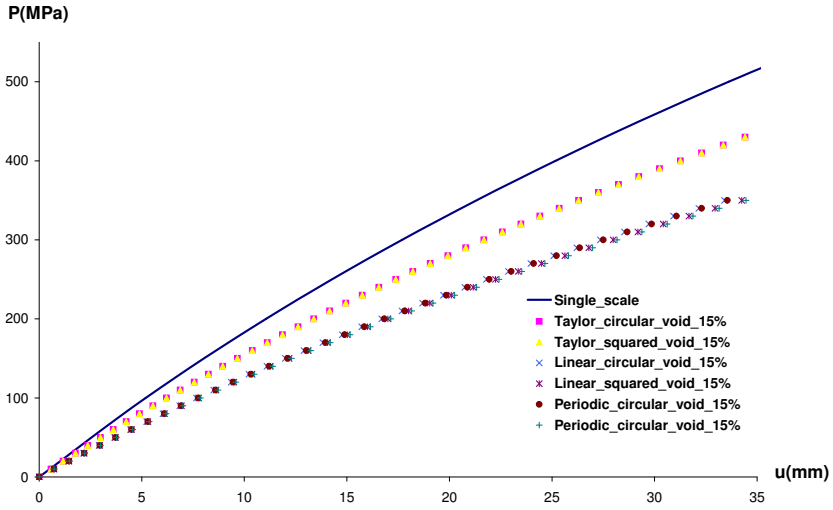

Figure 5: Internally pressurised hyperelastic cylinder. Pressure vs displacement diagram for full material and void at 15% volume fraction.

10.2. Mesh Evolution

In this section a mesh evolution is depicted to show how the different conditions affect the distortion during the micro-macro analysis. Macro- and micro-meshes are presented in its undeformed and deformed configurations, respectively. At every figure the deformed macro-mesh is translated radially and the deformed micro-mesh is translated in order to make the figures more transparent. In this way the strain experienced by both meshes can be observed clearly.

The meshes depicted in the deformed configurations all correspond to a similar outer radial displacement close to 3.5mm. For examples of 5% and 15% void fraction this deformation corresponds to an internal pressure $P = 450$MPa and $P = 350$MPa, respectively.

Figure 9(a) and 9(b) correspond to a Microstructure 1 (Circular void in the middle of the RVE with 5% volume fraction) for linear b.c. and periodic b.c., respectively. Figure 10(a) and 10(b) correspond to a

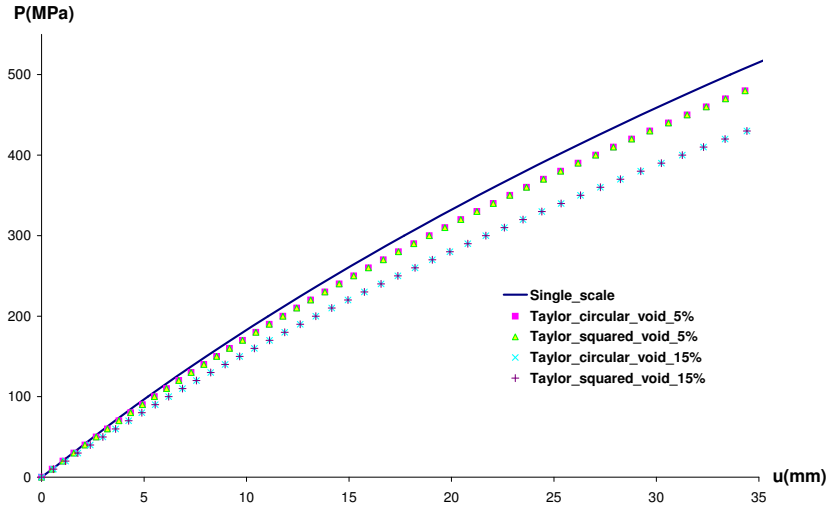

Figure 6: Internally pressurised hyperelastic cylinder. Pressure vs displacement diagram for the Taylor assumption

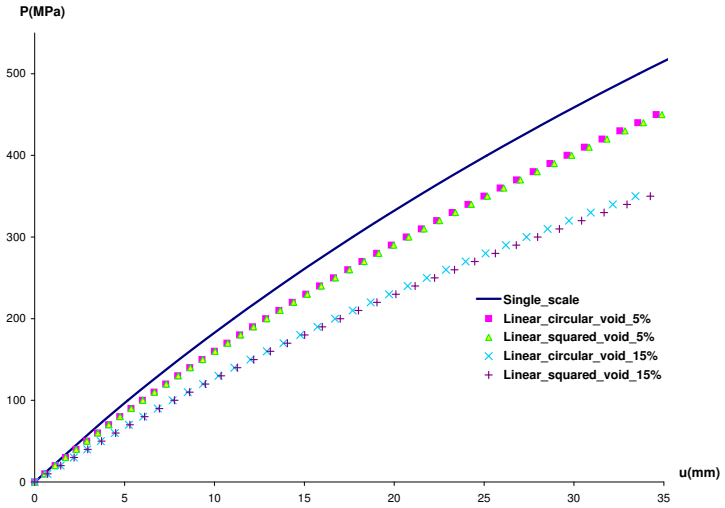

Figure 7: Internally pressurised hyperelastic cylinder. Pressure vs displacement diagram for the linear b.c.

Microstructure 2 (Square void in the middle of the RVE with 5% volume fraction) for linear and periodic b.c., respectively. We can observe that due to the small void there is only a small difference between Linear and Periodic b.c.

Figure 11(a) and 11(b) corresponds to a Microstructure 3 (Circular void in the middle of the RVE with 15% volume fraction) for Linear and Periodic b.c., respectively. Figure 12 correspond to a Microstructure 4 (Square void in the middle of the RVE with 15% volume fraction) for linear b.c. and periodic b.c., respectively. We can observe that due to a bigger void there is more difference between linear b.c. and periodic b.c. Moreover, the periodicity at periodic b.c. is observed easily.

10.3. Strain energy distribution

In this section several figures representing strain energy distributions (in KJ/mm^2) are depicted for a quarter of the cylinder with some representative microstructures. The distributions are depicted in the

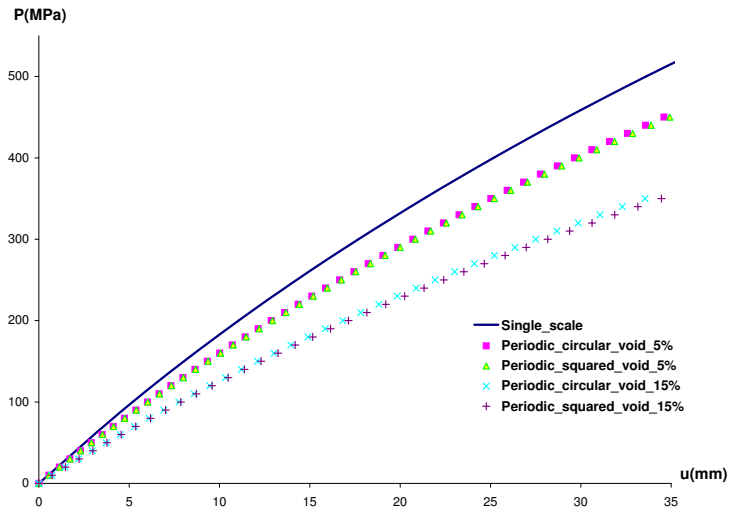

Figure 8: Internally pressurised hyperelastic cylinder. Pressure vs displacement diagram for the periodic b.c.

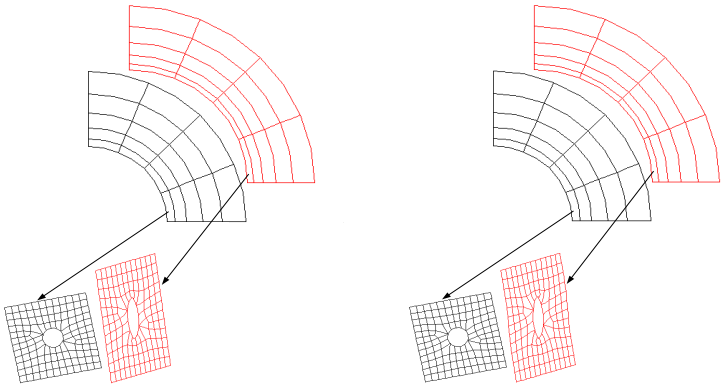

(a) Linear b.c. (b) Periodic b.c.

Figure 9: Mesh evolution for P=0-450MPa. Microstructure 1: circular void at 5% volume fraction

deformed configuration. The undeformed mesh is also depicted to illustrate more clearly deformation of the solid.

In Figure 13(a) and 13(b) the results for linear b.c. and periodic b.c. are represented for Microstructure 1, respectively, for internal pressure $P = 450$MPa. In Figure 14(a) and 14(b) the results for linear b.c. and periodic b.c. are represented for Microstructure 2, respectively, for internal pressure $P = 450$MPa. In Figure 15(a) and 15(b) the effect of linear b.c. and periodic b.c. is represented for Microstructure 3, respectively, for internal pressure $P = 350$MPa.

10.4. Residuals evolution per iteration in macro and micro levels

In this section tables with the Euclidean norm $\mathrm{R_M}$ of the residual are reported associated with the Newton iterations of the macro- and micro-equilibrium. The residual norm evolution is shown for the microstructure that corresponds to the macro Gauss point in the bottom right corner. In the following tables the Euclidean norm $\mathrm{R_M}$ of the residual are reported associated with the Newton iterations of the macro-equilibrium. The macro-residual is normalised and calculated as $\mathrm{R_M} = 100 \times \|\mathbf{F}_{int} - \mathbf{F}_{ext}\|/\|\mathbf{F}_{ext}\|$. The micro residual

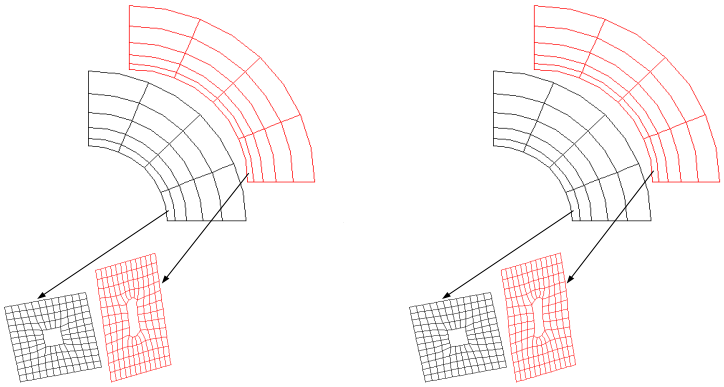

(a) Linear b.c. (b) Periodic b.c.

Figure 10: Mesh evolution for P=0-450MPa. Microstructure 2: square void at 5% volume fraction

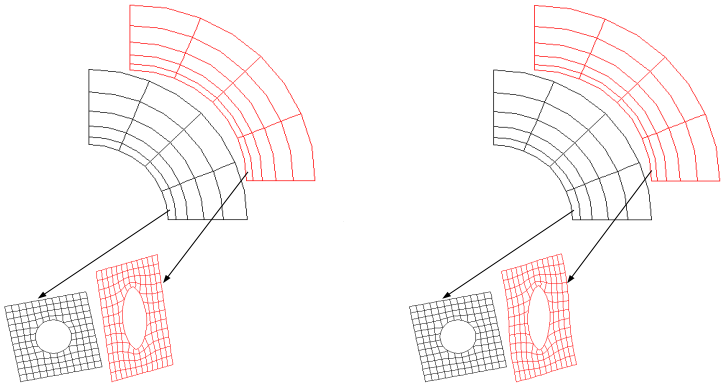

(a) Linear b.c. (b) Periodic b.c.

Figure 11: Mesh evolution for P=0-350MPa. Microstructure 3: circular void at 15% volume fraction

is computed in different ways depending on the constraint. The residual for linear b.c. is evaluated as $R_\mu = 100 \times \|\mathbf{r}\|/\|\mathbf{f}^{int}\|$. The residual for periodic b.c. is evaluated as $R_\mu = 100 \times \|\mathbf{r}\|/\|\mathbf{f}^{int}\|$. Clearly, the quadratic rate of asymptotic convergence is observed in the macro- and micro-scales for both Linear and Periodic b.c.'s in all the tables.

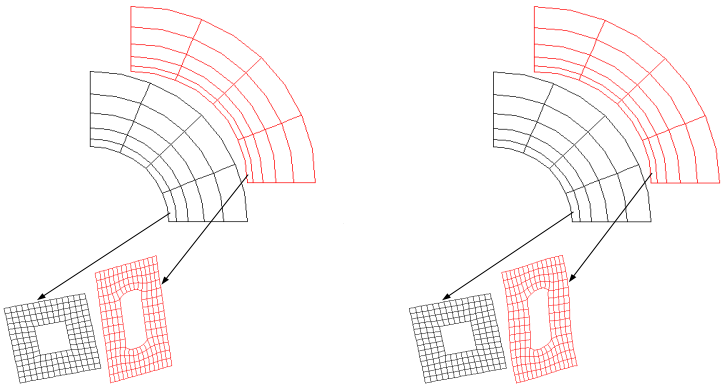

(a) Linear b.c. (b) Periodic b.c.

Figure 12: Mesh evolution for P=0-350MPa. Microstructure 4: square void at 15% volume fraction

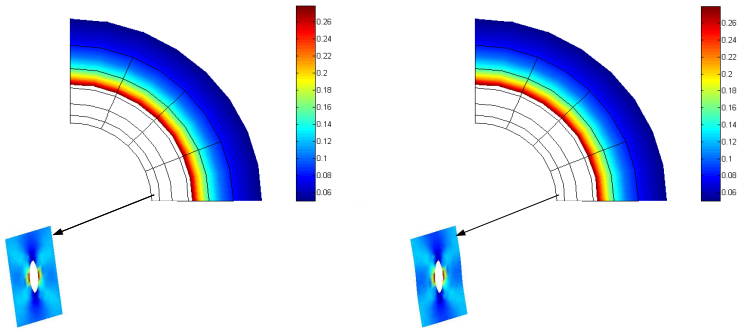

(a) Linear b.c. (b) Periodic b.c.

Figure 13: Strain energy for internal pressure $P = 450$ MPa. Microstructure 1: circular void at 5% volume fraction

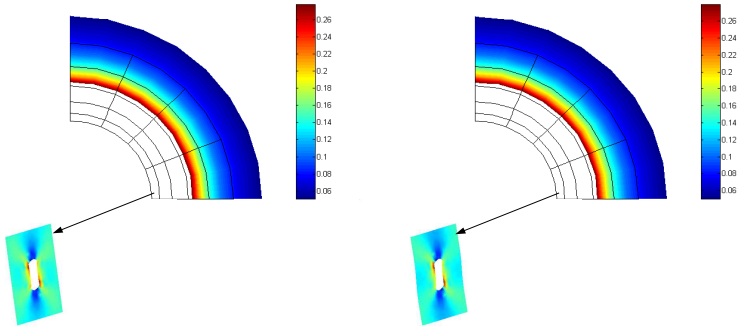

(a) Linear b.c. (b) Periodic b.c.

Figure 14: Strain energy for internal pressure $P = 450$ MPa. Microstructure 1: square void at 5% volume fraction

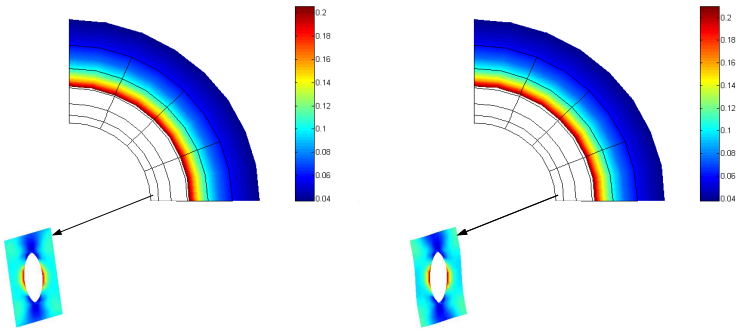

(a) Linear b.c. (b) Periodic b.c.

Figure 15: Strain energy for internal pressure $P = 350$ MPa. Microstructure 3: circular void at 15% volume fraction

micro	R_μ	Macro	R_M
1	3.054337×10^{-01}		
2	1.018779×10^{-03}		
3	2.642555×10^{-06}		
4	1.146325×10^{-08}	1	7.386827×10^{-01}
1	2.871463×10^{-01}		
2	4.395136×10^{-04}		
3	6.061724×10^{-07}		
4	1.207273×10^{-09}	2	5.075611×10^{-04}
1	2.870407×10^{-01}		
2	4.393127×10^{-04}		
3	6.059748×10^{-07}		
4	1.206522×10^{-09}	3	2.604021×10^{-07}
1	2.870407×10^{-01}		
2	4.393128×10^{-04}		
3	6.059750×10^{-07}		
4	1.206531×10^{-09}	4	1.912772×10^{-10}

a) Linear b.c.

micro	R_μ	Macro	R_M
1	3.020060×10^{-01}		
2	1.080160×10^{-03}		
3	2.773971×10^{-06}		
4	1.369076×10^{-08}	1	7.484814×10^{-01}
1	2.888288×10^{-01}		
2	4.713476×10^{-04}		
3	6.908600×10^{-07}		
4	1.495429×10^{-09}	2	5.070460×10^{-04}
1	2.887258×10^{-01}		
2	4.711845×10^{-04}		
3	6.907774×10^{-07}		
4	1.495436×10^{-09}	3	2.450213×10^{-07}
1	2.887258×10^{-01}		
2	4.711846×10^{-04}		
3	6.907774×10^{-07}		
4	1.495265×10^{-09}	4	1.739404×10^{-10}

b) Periodic b.c.

Table 1: Evolution of Residual norm at micro (R_μ) and Macroscale (R_M) for Linear b.c. and Periodic b.c. assuming Microstructure 2 (5% square void). Increment of internal pressure P = 200-201 MPa.

11. Conclusions

A novel formulation for multiscale finite element analysis of materials with microvoids undergoing large strains is proposed in this paper. The technique proved effective for the treatment of solids with different types of microvoids and its application to composite materials is deemed straightforward. **The antiperiodic traction conditions on the RVE within a large strain context provided a condensation technique which led to a formulation of tangent modulus necessary for embedment within an implicit numerical strategy**. The formulation thus posed led to *quadratic rates of convergence* under *periodic deformation* and *antiperiodic traction* on the boundary of RVE model. Numerical tests demonstrated the robustness and efficiency of the technique. **Taylor boundary condition (b.c) scheme is clearly showing some discrepancy respect the most accurate results obtained with linear and periodic. The results showed that there are no significant differences between linear and periodic bcs in terms of accurateness and in terms of convergence.**

References

[1] D. Peric, E.A. De Souza Neto, R.A. Feijo, M. Partovi, and A.J.C. Molina. On micro-to-macro transitions for multi-scale analysis of non-linear heterogeneous materials: Unified variational basis and finite element implementation. *International Journal for Numerical Methods in Engineering*, 87(1-5):149–170, 2011.

[2] Miehe C. Schotte J. and Schroder J. Computational micro-macro transitions and overall tangent moduli in the analysis of polycrystals at large strains. *Computational Material Science*, 16:372–382, 1999.

[3] Miehe C. and Koch A. Computational micro-to-macro transitions of discretized microstructures undergoing small strains. *Archive of Applied Mechanics*, 72:300–317, 2002.

[4] Nan C.W. and Clarke D.R. The influence of particle size and particle fracture o the elastic/plastic deformation of metal matrix composite. *Acta Materialia*, 44(9):3801–3811, 1996.

[5] Kouznetsova V.G. Brekelmans W.A.M. and Baaijens F.P.T. An approach to micro-macro modelling of heterogeneous materials. *Computational Mechanics*, 27:37–48, 2001.

[6] A.J. Carneiro Molina and J.L. Curiel-Sosa. A multiscale finite element technique for nonlinear multiphase materials. *Finite Elements in Analysis and Design*, 94:64–80, 2015.

[7] C. Reina, B. Li, K. Weinberg, and M. Ortiz. A micromechanical model of distributed damage due to void growth in general materials and under general deformationhistories. *International Journal for Numerical Methods in Engineering*, 93(6):575–611, 2013.

[8] Y. Aoyagi and K. Shizawa. A dislocation-crystal plasticity simulation on large deformation considering geometrically necessary dislocation density and incompatibility (2nd report, application to fcc single crystal). *Nihon Kikai Gakkai Ronbunshu, A Hen/Transactions of the Japan Society of Mechanical Engineers, Part A*, 72(11):1646–1653, 2006.

[9] M. Kastner, G. Haasemann, and V. Ulbricht. Multiscale xfem-modelling and simulation of the inelastic material behaviour of textile-reinforced polymers. *International Journal for Numerical Methods in Engineering*, 86(4-5):477–498, 2011.

[10] I. Watanabe, D. Setoyama, N. Nagasako, N. Iwata, and K. Nakanishi. Multiscale prediction of mechanical behavior of ferrite-pearlite steel with numerical material testing. *International Journal for Numerical Methods in Engineering*, 89(7):829–845, 2012.

[11] Gitman I.M. *Representative Volumes and Multi-scale Modelling of Quasi-brittle Materials*. PhD thesis, Technische Universiteit Delft, 2006.

[12] O. Lloberas-Valls, D. J. Rixen, A. Simone, and L. J. Sluys. Multiscale domain decomposition analysis of quasi-brittle heterogeneous materials. *International Journal for Numerical Methods in Engineering*, 89(11):1337–1366, 2012.

[13] V. P. Nguyen, O. Lloberas-Valls, M. Stroeven, and L. J. Sluys. Computational homogenization for multiscale crack modeling. implementational and computational aspects. *International Journal for Numerical Methods in Engineering*, 89(2):192–226, 2012.

[14] C. Oskay. Two-level multiscale enrichment methodology for modeling of heterogeneous plates. *International Journal for Numerical Methods in Engineering*, 80(9):1143–1170, 2009.

[15] P. Ladeveze. Multiscale modelling and computational strategies for composites. *International Journal for Numerical Methods in Engineering*, 60(1):233–253, 2004.

[16] B. N. Nguyen and K. L. Simmons. A multiscale modeling approach to analyze filament-wound composite pressure vessels. *Journal of Composite Materials*, 47(17):2113–2123, 2013.

[17] S. Marfia and E. Sacco. Analysis of sma composite laminates using a multiscale modelling technique. *International Journal for Numerical Methods in Engineering*, 70(10):1182–1208, 2007.

[18] Torquato S. *Random Heterogeneous Materials. Microestructure and Macroscopic Properties*. Springer, 2002.

[19] F.J. Vernerey and M. Kabiri. Adaptive concurrent multiscale model for fracture and crack propagation in heterogeneous media. *Computer Methods in Applied Mechanics and Engineering*, 276:566–588, 2014.

[20] V. Peron-Luhrs, F. Sansoz, A. Jrusalem, and L. Noels. Multiscale computational modeling of deformation mechanics and intergranular fracture in nanocrystalline copper. *Computational Materials Science*, 90:253–264, 2014.

[21] M. Kabiri and F.J. Vernerey. An xfem based multiscale approach to fracture of heterogeneous media. *International Journal for Multiscale Computational Engineering*, 11(6):565–580, 2013.

[22] N. Zhang, J. Yao, Z. Huang, and Y. Wang. Accurate multiscale finite element method for numerical simulation of two-phase flow in fractured media using discrete-fracture model. *Journal of Computational Physics*, 242:420–438, 2013.

[23] R.A. Regueiro and S.-K. Yu. Finite-element analysis of grain-matrix micro-cracking in shale within the context of a multiscale modeling approach for fracture. *International Journal for Multiscale Computational Engineering*, 10(5):407–424, 2012.

[24] C.V. Verhoosel, J.J.C. Remmers, and M.A. Gutirrez. A partition of unity-based multiscale approach for modelling fracture in piezoelectric ceramics. *International Journal for Numerical Methods in Engineering*, 82(8):966–994, 2010.

[25] C. Gonzalez and J. Llorca. Multiscale modeling of fracture in fiber-reinforced composites. *Acta Materialia*, 54(16):4171–4181, 2006.

[26] Miehe C. and Dettmar J. A framework for micro-macro transitions in periodic particle aggregates of granular materials. *Computer Methods in Applied Mechanics and Engineering*, 193:225–256, 2004.

[27] E. W. C. Coenen, V. G. Kouznetsova, and M. G. D. Geers. Computational homogenization for heterogeneous thin sheets. *International Journal for Numerical Methods in Engineering*, 83(8-9):1180–1205, 2010.

[28] V. K. Lai, M. F. Hadi, R. T. Tranquillo, and V. H. Barocas. A multiscale approach to modeling the passive mechanical contribution of cells in tissues. *Journal of Biomechanical Engineering*, 135(7), 2013.

[29] M. Marino and G. Vairo. Stress and strain localization in stretched collagenous tissues via a multiscale modelling approach. *Computer Methods in Biomechanics and Biomedical Engineering*, 17(1):11–30, 2014.

[30] A. Abdulle. On a priori error analysis of fully discrete heterogeneous multiscale fem. *Multiscale Modeling and Simulation*, 4(2):447–459, 2005.

[31] R. Tian, A. C. To, and W. K. Liu. Conforming local meshfree method. *International Journal for Numerical Methods in Engineering*, 86(3):335–357, 2011.

[32] Miehe C. Computational micro-to-macro transitions for discretized micro-structures of heterogeneous materials at finite strains based on the minimization of averaged incremental energy. *Computer Methods in Applied Mechanics and Engineering*, 192:559–591, 2003.

[33] Hill R. On constitutive macro-variables for heterogeneous solids at finite strain. *Proceeding of the Royal Society of London*, 326:131–147, 1972.

[34] Miehe C. Schroder J. and Schotte J. Computational homogenization analysis in finite plasticity. simulation of texture development in polycrystalline materials. *Computer Methods in Applied Mechanics and Engineering*, 171:387–418, 1999.